

# Dark-Matter-Deficient Galaxies from Collisions: A New Probe of Bursty Feedback and Dark Matter Physics

YI-YING WANG ,<sup>1</sup> DANENG YANG ,<sup>1,2</sup> KEYU LU,<sup>1</sup> YUE-LIN SMING TSAI ,<sup>1,2</sup> AND YI-ZHONG FAN ,<sup>1,2</sup>

<sup>1</sup>Key Laboratory of Dark Matter and Space Astronomy, Purple Mountain Observatory, Chinese Academy of Sciences, Nanjing 210033, People's Republic of China

<sup>2</sup>School of Astronomy and Space Science, University of Science and Technology of China, Hefei, Anhui 230026, People's Republic of China

## ABSTRACT

High-velocity collisions between gas-rich ultra-diffuse galaxies present a promising formation channel for dark-matter-deficient galaxies (DMDGs). Using hydrodynamical simulations, we show that the progenitors' baryonic binding energy,  $|E_{\text{bind}}|$ , critically controls the outcome. Repeated potential fluctuations, e.g., from bursty feedback, inject energy and reduce  $|E_{\text{bind}}|$  by  $\approx 15\%$ , yielding fewer but substantially more massive DMDGs. By contrast, elastic self-interacting dark matter (SIDM) produces comparable cores without lowering  $|E_{\text{bind}}|$ , resulting in negligible effect. This differs from the other DMDG formation scenario, where SIDM-induced cores enhance dark matter tidal stripping while keeping baryons compact and resilient to tidal effects. The contrasting roles of SIDM help distinguish feedback-formed halo cores from those created by SIDM. Among 15 paired simulation runs, 13 show higher DMDG masses in the weakened-binding case, and about two thirds exhibit  $> 100\%$  mass enhancements. The simulations also predict systematically lower gas fractions due to sustained post-collision star formation, yielding a clean observational signature. Upcoming wide-field imaging (CSST, LSST), HI surveys (FAST), and kinematic follow-up will be crucial to test this scenario.

## 1. INTRODUCTION

Within the standard cosmological model, the cosmic baryon fraction is only one-fifth that of the dark matter, and galaxies are expected to reside in more massive dark matter halos. As a result of galaxy formation governed by complex processes, the dark matter content of typical dwarf galaxies is expected to exceed their stellar mass by roughly two orders of magnitude (A. Dekel & J. Silk 1986; P. F. Hopkins et al. 2014; A. Vale & J. P. Ostriker 2004; P. S. Behroozi et al. 2013).

In this context, the observation of galaxies with exceptionally low dark matter content challenges the  $\Lambda$ CDM framework (P. van Dokkum et al. 2018, 2019; Q. Guo et al. 2019; P. E. Piña Mancera et al. 2022; S. Comerón et al. 2023). A notable case is NGC 1052-DF2 and DF4 (P. van Dokkum et al. 2018, 2019), commonly described as dark-matter-deficient galaxies (DMDGs). Both of these are ultra-diffuse systems, with velocity dispersion measurements consistent with little or no dark matter. Proposed formation scenarios include tidal stripping in cored halos (G. Ogiya 2018; D. Yang et al. 2020; L. V. Sales et al. 2020; Z.-C. Zhang et al. 2025a,b) and high-velocity collisions that produce dark-matter-deficient remnants (P. van Dokkum et al. 2022; J. Lee et al. 2024; M. A. Keim et al. 2025). Notably, Q. Guo et al. (2019) identified 19 DMDGs from a sample of 324 SDSS dwarfs, with 14 located well beyond the virial radii of nearby groups or clusters, where environmental stripping and recent interactions are unlikely.

Existing cosmological simulation studies have identified DMDGs as tidally stripped satellites (J. Moreno et al. 2022; Y. Jing et al. 2019). In this scenario, controlled simulations further map the orbital conditions and galaxy-halo configurations required to form such systems, offering a way to test models of elastic self-interacting dark matter (SIDM) that produce cored halos without making baryons too diffuse (D. Yang et al. 2020). However, the identification of DMDGs in isolation remains challenging, hindered by the competing requirements for both high resolution and a large field of view. Recently, J. Lee et al. (2024) used the TNG100-1 simulation (D. Nelson et al. 2019) to search for gas-rich dwarf pairs whose orbital parameters satisfy requirements for producing DMDGs near massive hosts, finding

$\sim 10$  such collisions in a  $(100 \text{ Mpc})^3$  volume over  $z \simeq 3 \rightarrow 0$ . The mass and spatial resolution of TNG100 are insufficient to follow the hydrodynamics required to produce such systems, but the implied event rate broadly agrees with the handful of field DMDGs reported by Q. Guo et al. (2019), suggesting that dwarf-dwarf collisions provide a cosmologically plausible channel for generating observable DMDGs. Though how collision velocity, disk structure, and initial configuration affect the DMDG formation has been examined in some recent simulations (E.-j. Shin et al. 2020; J. Lee et al. 2024), it remains unclear what physical quantity critically controls the mass and yield of DMDGs.

In this work, we identify the baryonic binding energy of the progenitors,  $|E_{\text{bind}}$ , as the relevant control parameter, directly linking energy injection in dwarf halos to DMDG yields. We employ controlled hydrodynamical simulations of gas-rich ultra-diffuse galaxy (UDG) collisions to assess the potential of these systems as probes of energy injection in dwarf halos, positioning DMDG observations a new observational window for testing the underlying physics. Intriguingly, both baryonic feedback (J. F. Navarro et al. 1996; S. Mashchenko et al. 2006; F. Governato et al. 2010) and self-interacting dark matter (SIDM) (D. N. Spergel & P. J. Steinhardt 2000; S. Tulin & H.-B. Yu 2018) have been proposed as mechanisms for generating cores in halos, but their consequences diverge remarkably in collisional events. Future DMDG studies can thus inform both galaxy formation and dark sector physics.

## 2. WEAKENING GRAVITATIONAL BINDING BY ENERGY INJECTION.

To unbind baryons from halos more efficiently, we need processes that reduce the gravitational binding of the entire system. Although energy injection into halos can weaken the binding of their baryonic component, most baryonic processes, such as gas cooling, release their energy radiatively, thereby dissipating rather than adding energy to the gravitationally bound system. In contrast, repeated potential fluctuations can heat dark matter in the inner regions, reducing the gravitational binding after relaxation and flattening the inner halo density profile. Such fluctuations arise naturally from bursty stellar feedback in dwarf galaxies (A. Pontzen & F. Governato 2012; T. K. Chan et al. 2018; J. Freundlich et al. 2020; Z. Li et al. 2023). In novel dark matter models, recurrent collapses of solitonic cores can trigger bosenova-like outbursts that drive similar fluctuations (P. J. Fox et al. 2023; H. Koo 2025). Scattering among dark matter particles may also be exothermic, imparting kinetic energy to the final-state particles while keeping them bound to the halo (M. Vogelsberger et al. 2019; M. V. Medvedev 2014).

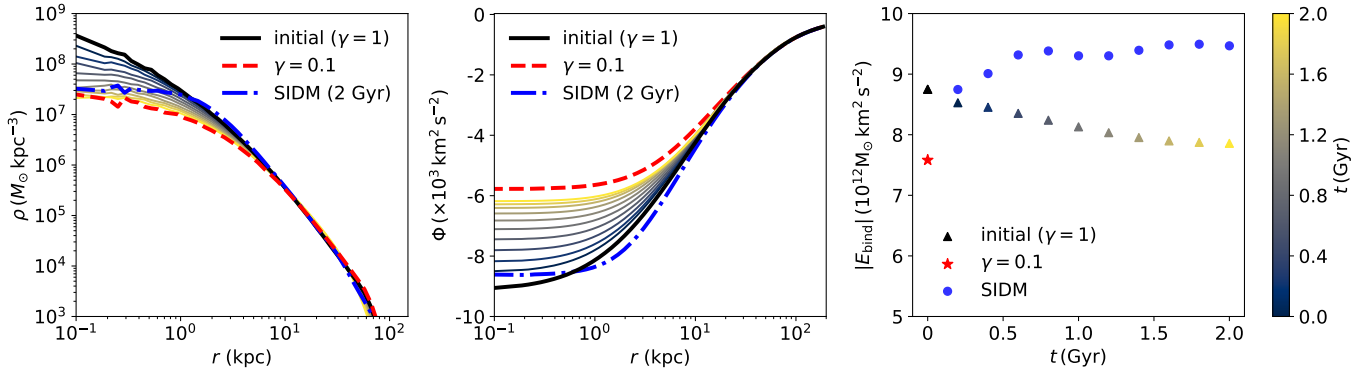


**Figure 1. Effect of energy injection into dark matter halos.** Repeated potential variations, such as those induced by bursty feedback, can flatten the inner halo densities (left), shallow the potential (middle), and decrease the absolute baryonic binding energy,  $|E_{\text{bind}}$  (right). The final snapshot resembles a  $\gamma = 0.1$  (red) profile, which features an inner density core and a reduced  $|E_{\text{bind}}$  relative to the initial cuspy  $\gamma = 1$  profile (black), and we adopt this in our simulations. For comparison, we overlay SIDM results (blue) from a simulation with the same initial  $\gamma = 1$  condition and a cross section per mass  $\sigma/m = 20 \text{ cm}^2/\text{g}$ . The initial conditions correspond to the 1a and 1b benchmarks listed in Equation 1.

As a quantitative illustration, we model the evolution of a halo density profile under energy injection, following the method of A. Pontzen & F. Governato (2012), which has been widely applied in various contexts (A. Pontzen & F. Governato 2012; A. Di Cintio et al. 2014; S. Peirani et al. 2017; J. F. Acevedo et al. 2024). For demonstration, we present results for a spherical, isotropic NFW halo with a mass of  $1.5 \times 10^{10} \text{ M}_\odot$  and a concentration parameter of  $c = 14$ , corresponding to the 1a and 1b benchmarks in Equation 1. For each dark matter particle, we compute the total energy  $E_0$  and specific angular momentum  $j$ . A sequence of impulsive potential fluctuations is modeled by rescaling the potential by a small fraction,  $\Delta V/V_0 = 0.14$ , at each iteration. The energy of each particle is updated using the

**Table 1.** Representative simulation benchmarks.

BM	Profile	$v_r$ (km/s)	$ \frac{\Delta E_{\text{bind}}}{E_{\text{bind}}(\gamma=1)} $	$\frac{M_b(\gamma=0.1)}{M_b(\gamma=1)}$
1a	$\gamma = 1$	400	0.13	7.20
1b	$\gamma = 0.1$	400	0.08	1.83
1c	SIDM	400	0.08	1.83
2a	$\gamma = 1$	400	0.15	5.74
2b	$\gamma = 0.1$	400	0.15	2.53
3a	$\gamma = 1$	280	0.15	2.53
3b	$\gamma = 0.1$	280	0.15	2.53

NOTE—The full simulation parameters and numerical results are provided in the Materials and Methods section.

phase-averaged kick at fixed  $j$

$$\Delta E = \frac{2nE_0}{(2+n)^2} \left( \frac{\Delta V}{V_0} \right)^2, \quad (1)$$

where  $n = 2$  represents a harmonic oscillator potential. After each impulse, we advance the simulation time by 0.2 Gyr and reconstruct the density profile by summing the orbit-averaged radial probability distributions

$$p(r; E, j) \propto \frac{1}{\sqrt{E - V_{\text{eff}}(r, j)}}, \quad (2)$$

$$V_{\text{eff}}(r, j) = V(r) + \frac{j^2}{2r^2}, \quad (3)$$

over all dark matter particles. The baryon content is assumed to be a gas disk which takes spherically averaged pseudo-isothermal profile,  $\rho_{\text{gas}} = \rho_0 (1 + (r/r_g)^2)^{-1}$ , where  $r_g = 2$  kpc and  $\rho_0 = 2.46 \times 10^6 \text{ M}_\odot \text{ kpc}^{-3}$  (S. Kurapati et al. 2020; J. Lee et al. 2024). The disk height is set to 0.2 kpc.

Figure 1 shows the evolution of the density profile (left), gravitational potential (middle), and  $|E_{\text{bind}}|$  (right) in 2 Gyr. We compute  $E_{\text{bind}}$  by integrating the gas density over the total gravitational potential ( $\Psi_{\text{tot}}$ ),  $E_{\text{bind}} = 4\pi \int dr r^2 \Psi_{\text{tot}} \rho_{\text{gas}}$ . The results illustrate that impulsive feedback heats the inner orbits, leading to an expansion of centrally cored density profile, a shallowing of the central potential, and a reduction in the central baryonic binding energy. By 2 Gyr,  $|E_{\text{bind}}|$  has decreased by over 10%. We will use collision simulations to show that even this modest reduction can substantially enhance the DMDG formation.

We also contrast this with the effect of SIDM, a distinct core formation mechanism. To this end, we simulate the same initial condition as in the 1a and 1b benchmarks (Equation 1), considering only gravity and using the **Gadget-2**-based SIDM module developed in D. Yang & H.-B. Yu (2022) and D. Yang et al. (2023), adopting a cross section of  $\sigma/m = 20 \text{ cm}^2 \text{ g}^{-1}$ . In Figure 1, the evolved density profile at 2 Gyr is shown in gray. While the SIDM halo develops a core of comparable size to that formed by feedback, its gravitational potential remains deep, and  $|E_{\text{bind}}|$  slightly increases rather than decreases. This suggests that baryonic binding, if quantified observationally, could serve as a diagnostic to distinguish between the two core formation mechanisms.

Equation 1 summarizes the configurations and results of representative simulations. The labels  $\gamma = 0.1$  and  $\gamma = 1$  correspond to simulations with and without weakened baryonic gravitational binding. We model the density profiles using an extended NFW profile with an inner slope controlled by the parameter  $\gamma$  (see Materials and Methods for details).

### 3. SIMULATION SETUP

To illustrate the impact of energy injection into halos in a model-independent manner, we adopt the following NFW-like extension for the halo density profile (A. W. Graham et al. 2006; G. Ogiya 2018)

$$\rho(r) = \frac{\rho_s}{\left( \frac{r}{r_s} \right)^\gamma \left( 1 + \frac{r}{r_s} \right)^{3-\gamma}}, \quad (4)$$

where the central density slope is governed by  $\gamma$ , with smaller values of  $\gamma$  corresponding to less gravitationally bound halos.

We construct two contrasting sets of initial conditions, one with  $\gamma = 1$  (cuspy) and the other with  $\gamma = 0.1$  (cored, with weaker binding), while keeping the total halo mass and concentration fixed. The simulated halos span masses of  $1 - 2 \times 10^{10} M_{\odot}$  and concentrations in the range  $4 - 14$ . Assuming these halos host gas-rich UDGs, we model the baryonic content with a gas-only disk, as described previously, and vary the disk height between 0.15 and 0.35 kpc. This maximizes the effectiveness of DMDG formation, as stars behave as a collisionless component during the collision and cannot be efficiently expelled from the progenitors. The gas-to-halo mass ratio is set to 0.1 or 0.22, with gas scale radii  $r_g$  in the range 1.5 – 3.5 kpc. The pericentric distance is assumed to be 2 kpc. These choices are motivated by observations of gas-rich UDGs, where internal turbulence and stellar feedback maintain gas densities below the threshold for molecular hydrogen formation,  $n_g \lesssim 1 \text{ cm}^{-3} \approx 3 \times 10^7 M_{\odot} \text{kpc}^{-3}$ , thereby suppressing star formation (A. Di Cintio et al. 2017; T. K. Chan et al. 2018). The population and properties of gas-rich UDGs have attracted considerable attention and been extensively explored in recent studies (E. Papastergis et al. 2017; F. Jiang et al. 2019; T. K. Chan et al. 2018; M. G. Jones et al. 2018; P. E. Mancera Piña et al. 2020; D. Kong et al. 2022).

Equilibrium initial conditions are generated using DICE (V. Perret et al. 2014), with the gas disk stabilized by enforcing a Toomre  $Q_{\text{gas}} > 1.5$  (A. Toomre 1964; J. Binney & S. Tremaine 2008; D. Williamson et al. 2016). The gas is initialized at  $T = 10^4$  K and metallicity  $Z = 0.1 Z_{\odot}$ . We evolve the collision simulations using Gadget-4 (V. Springel et al. 2021), incorporating radiative cooling of primordial gas and star formation based on the multiphase ISM model of V. Springel & L. Hernquist (2003). Stellar feedback is modeled as an effective pressure that prevents the gas from collapsing too quickly. To obtain the SIDM prediction, we set up a hydrodynamical CDM simulation using progenitors taken from the isolated SIDM simulation (Gadget-2) snapshot at 2 Gyr. We verified that switching off SIDM after this initialization yields a stationary profile in isolation. Further details are provided in the Supplementary Material.

Our collision simulations build upon findings in previous studies, where dependencies of simulation outcomes on the collision velocities, progenitor halo mass and concentration, gas distribution, and numerical resolution were systematically explored. We adopt simulation setups similar to those in E.-j. Shin et al. (2020) and J. Lee et al. (2024), with relative collision velocities ( $v_r$ ) ranging from 300 – 600 km/s. Our primary choice of  $v_r = 400$  km/s lies within the preferred range reported in the literature. We also perform simulations with  $v_r = 280, 450$  and 500 km/s. The two colliding progenitors are initialized with identical conditions, placed at a separation of 60 kpc along their relative velocity vector and with an impact parameter of 2 kpc. We focus on contrasting paired samples with  $\gamma = 1$  and  $\gamma = 0.1$ , testing them under a range of conditions. Table 2 summarizes the initial conditions and parameter setup in our simulations.

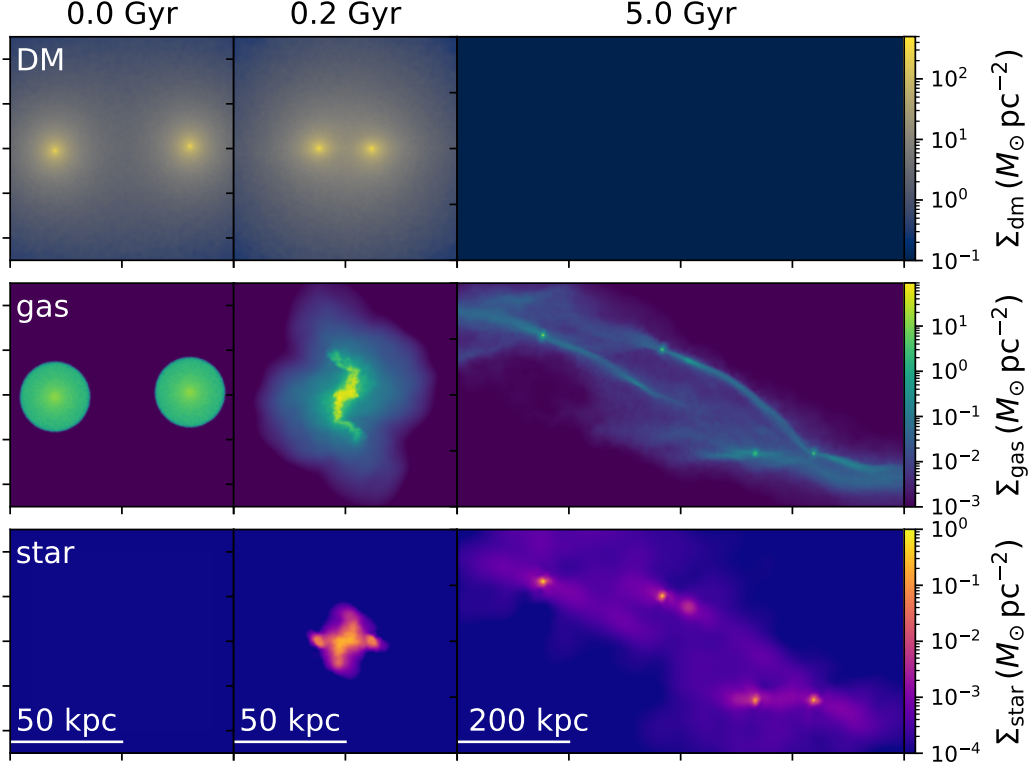
#### 4. COLLISIONAL FORMATION OF DMDGS.

Figure 2 shows simulation snapshots of the surface densities of dark matter (top), gas (middle), and stars (bottom) for the benchmark 2a ( $\gamma = 1$ ) in Equation 1. Four stages of the collision are displayed. The first snapshot depicts the initial setup, with two progenitors approaching each other at close separation so that the simulation outcome primarily concerns the formation of DMDGs rather than the internal dynamics of the progenitors. The systems collide within 0.2 Gyr, displacing their gas from the halo centers and triggering efficient star formation. By 5 Gyr, the expelled baryons have already collapsed into several DMDGs and moved far from their progenitors.

With  $v_r = 400$  km/s, most of the progenitor gas is expelled. In the cuspy case ( $\gamma = 1$ ), the steeper dark-matter potential exerts stronger tidal “winds,” causing the expelled gas to fragment into several small, low-mass condensations. In contrast, in the weakened-binding case ( $\gamma = 0.1$ ), the debris remains in contact more easily, allowing it to coalesce into fewer but more massive DMDGs.

To quantify how the tide acts on an extended gas debris, we evaluate on the mid plane the largest eigenvalue ( $\lambda_{\text{max}}$ ) of the tidal tensor  $T \equiv -\nabla \nabla \Phi$ , for which negative eigenvalues imply convergent relative acceleration. Figure 3 shows the head-on collisions between two identical progenitor halos, using parameters from the first benchmark in Equation 1, at varying separations:  $d = 0$  (left), 4 (middle), and 8 kpc (right) for the  $\gamma = 1$  (top),  $\gamma = 0.1$  (middle), and SIDM (bottom) cases. We highlight the  $\lambda_{\text{max}} = 0$  contour, within which all eigenvalues are negative and the tide is compressive.

The  $\gamma = 0.1$  model develops broad, contiguous compressive regions around the origin across all separations, consistent with debris that readily coalesces into fewer, more massive clumps. A shallower inner slope renders the central potential more nearly harmonic, weakens shear, and suppresses stretching along the collision axis. By contrast, the cuspy



**Figure 2. Formation of DMDGs from the collision of gas-rich dwarf galaxies.** The initial setup (left) has two progenitors approaching at a close separation. They collide within 0.2 Gyr (middle), displacing gas from the halo centers and triggering efficient star formation. By 5 Gyr (right), the expelled baryons have collapsed into several DMDGs that are far from their progenitors. The surface density distributions of dark matter (top), gas (middle), and stars (bottom) are presented at the corresponding snapshots for the 2a ( $\gamma = 1$ ) benchmark.

$\gamma = 1$  case exhibits only small, fragmented compressive islands around shear-dominated zones, consistent with the formation of multiple low-mass condensations. The SIDM core is encircled by a ring of stretching tides that inhibits gas confinement. The central compressive region still facilitates gas condensation, but the formation of DMDG is significantly suppressed compared with the  $\gamma = 0.1$  scenario.

In a weakened gravitational binding scenario, gas is expected to escape more readily during collisions. To illustrate this, we reduce the collision velocity of the 3a and 3b benchmarks to 280 km/s (see Equation 1 for setup and results). The escaping gas mass reaches  $3.8 \times 10^9 M_\odot$  in the  $\gamma = 0.1$  case, compared to  $3.3 \times 10^9 M_\odot$  for  $\gamma = 1$ . Both the stellar and gas masses bound to the resulting DMDGs are substantially higher in the  $\gamma = 0.1$  scenario, with enhancements of 240% and 34%, respectively. The most massive DMDG formed in our simulations has a stellar mass of  $1.68 \times 10^9 M_\odot$ , obtained in the  $\gamma = 0.1$ ,  $v_r = 280$  km/s run. These results demonstrate that reduced baryonic binding favors the formation of more massive DMDGs.

Aside from the examples shown, we simulated 15 pairs of dwarf collisions with varied setups. Figure 4 presents the relative DMDG mass enhancements in the  $\gamma = 0.1$  and  $\gamma = 1$  cases, with bar widths proportional to the reduction in baryonic binding energy and colors indicating the gas fraction,  $f = M_{\text{gas}}/(M_{\text{gas}} + M_{\text{stars}})$ . We find that 13 of the 15 simulations yield an increase in DMDG mass, with 9 of these cases showing an enhancement greater than 100%. The two exceptions occur for halos with extremely low concentrations ( $c = 4$ ) and  $v_r = 450$  km/s, conditions that reduce the contrast between the two scenarios. Interestingly, the gas fractions in the  $\gamma = 0.1$  runs are systematically lower than in their  $\gamma = 1$  counterparts, demonstrating more sustained star formation following the collision. In this figure, we illustrate results considering only the most massive DMDGs. Our findings remain largely unchanged when considering the sum of multiple DMDG masses. The Materials and Methods section presents analogous results that include the total DMDG mass as well as the case with the gas cooling rate reduced by half. Additional details on post-collision star formation are also provided.

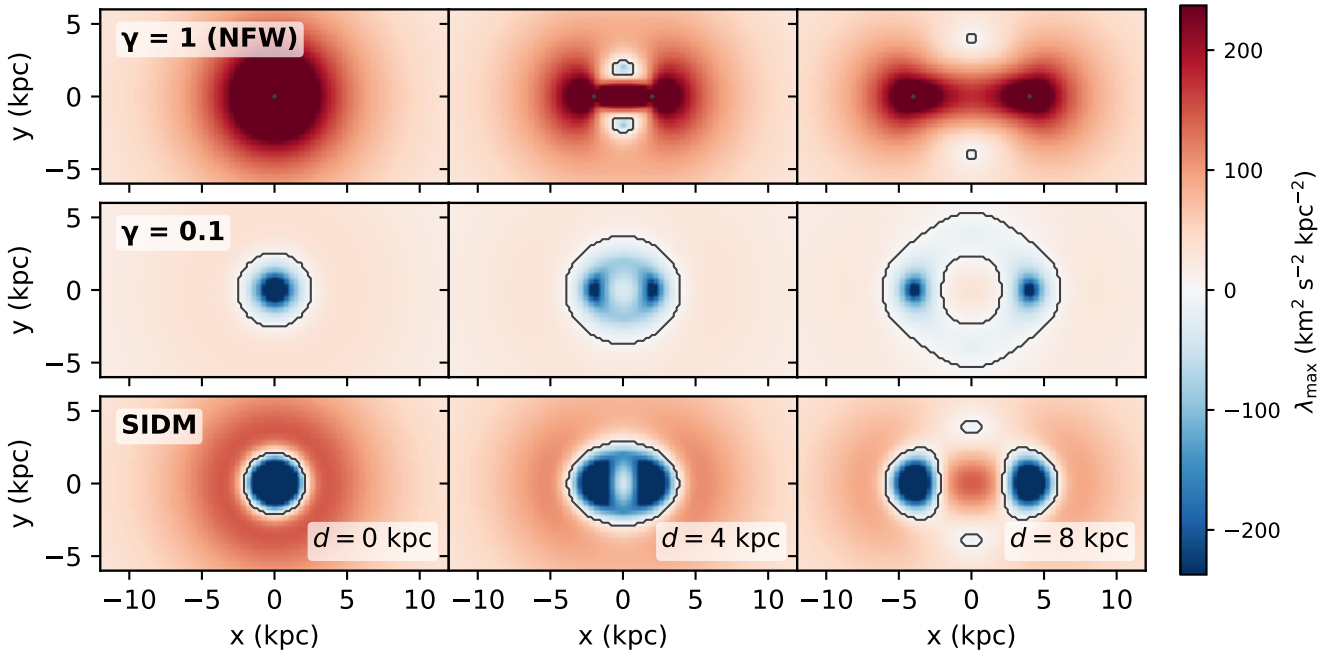


**Figure 3. Effect of tides on extended gas debris.** The figure shows the largest eigenvalue ( $\lambda_{\max}$ ) of the tidal tensor on the mid-plane for halo pairs with inner slopes of  $\gamma = 1$  (top),  $\gamma = 0.1$  (middle), and a cored SIDM profile (bottom), displayed at separations of  $d = \{0, 4, 8\}$  kpc (columns). Warm colors denote tidal stretching along at least one principal direction ( $\lambda_{\max} > 0$ ), while cold colors indicate fully compressive tides with all eigenvalues negative ( $\lambda_{\max} < 0$ ). The halo parameters follow the first benchmark listed in Table 1.

## 5. DISCUSSION AND CONCLUSION

Our controlled simulations show that energy injection weakens the progenitors' baryonic binding, elevating DMDG formation through collisions. Repeated potential fluctuations, as expected from bursty stellar feedback, may reduce  $|E_{\text{bind}}|$  by only 15%, yet in two thirds of the simulations, the DMDG masses are enhanced by over 100%. In contrast, SIDM creates cores without lowering  $|E_{\text{bind}}|$  and has a negligible effect on DMDG masses.

In the regime of high mass ratios and low collision velocities, close encounters between satellite and host galaxies have been proposed as a primary channel for producing DMDGs within host systems (J. Moreno et al. 2022; D. Yang et al. 2020; Y. Jing et al. 2019; G. Ogiya 2018). In such interactions, however, tidal stripping acts on both the dark matter and baryonic components of the satellite. If baryonic feedback is too strong, it can make the baryons too diffuse and easily stripped, hindering the formation of DMDGs. In contrast, SIDM can generate cores without significantly expanding the stellar distribution, offering a more efficient mechanism for DMDG formation (D. Yang et al. 2020). The relative abundance of DMDGs in the field versus those in host halos thus provides a potential observational handle to distinguish between core formation driven by baryonic feedback and that induced by SIDM.

The distinct formation pathways of DMDGs lead to contrasting observational signatures. Systems produced through tidal stripping resemble ordinary satellites but typically exhibit lower surface brightness. In contrast, those formed from post-collision tidal debris contain a substantial stellar component with nearly uniform ages and metallicities, created in a short burst at the time of the encounter. Another class of baryon-dominated systems is the tidal dwarf galaxy, which forms from tidal-tail gas ejected during a strong interaction involving a massive disk (F. Bournaud & P. A. Duc 2006; G. Gentile et al. 2007; S. Kaviraj et al. 2012; J. Zaragoza-Cardiel et al. 2024). These galaxies are typically embedded within tidal tails and generally lack bright globular clusters (J. Lee et al. 2024).

Future observations of such systems will be highly informative. Wide-field surveys (LSST, WFST, CSST, Roman, Euclid) will significantly expand the catalogs of low-surface-brightness galaxies and enable the identification of DMDG candidates through their morphologies, stellar populations, and associated globular clusters. Crucially, 21-cm surveys (FAST, MeerKAT, VLA) will measure gas fractions and kinematics, confirming whether baryons alone can account for the observed dynamics.

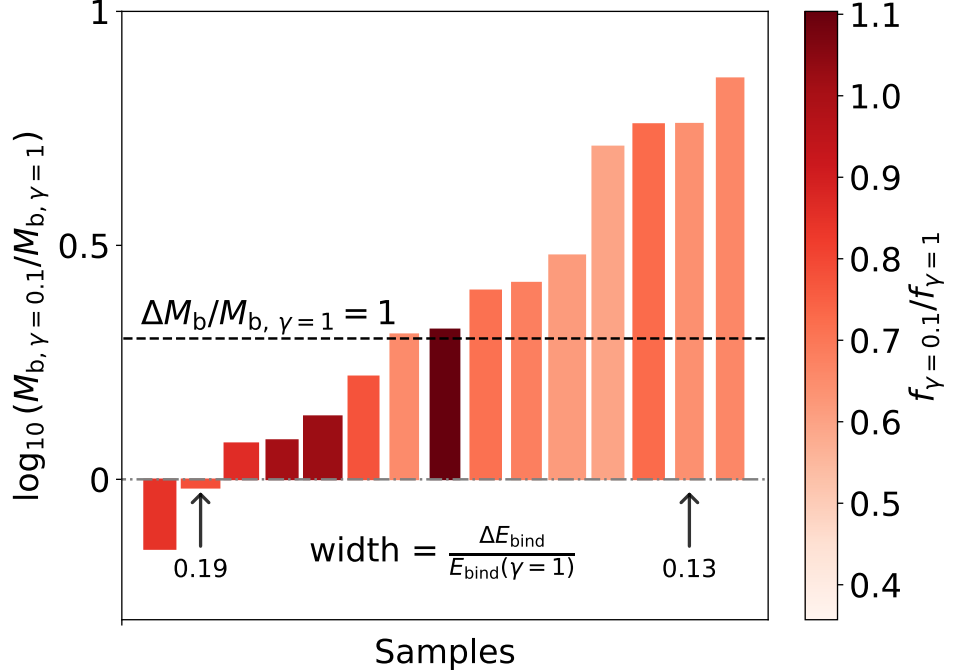


**Figure 4. Characteristics of the most massive DMDGs in 15 paired simulations.** The bar chart summarizes results from contrasting simulations with inner slopes  $\gamma = 0.1$  and  $\gamma = 1$ . Bars are arranged in ascending order of the DMDG mass ratio,  $M_{b,\gamma=0.1}/M_{b,\gamma=1}$ . The bar width scales with the relative change in binding energy,  $(E_{\text{bind},\gamma=1} - E_{\text{bind},\gamma=0.1})/E_{\text{bind},\gamma=1}$ , while the color indicates the gas fraction,  $f = M_{\text{gas}}/(M_{\text{gas}} + M_{\text{stars}})$ . In contrast, the increase in the DMDG masses is predominantly positive. In 9 out of the 15 simulations, this increase exceeds 100%, as reflected by the bars that rise above the line representing  $\Delta M_b/M_{b,\gamma=1} = 1$ .

Extending this analysis to more realistic and cosmological settings will be essential for quantifying the DMDG population both in the field and within host environments. However, meeting the simultaneous demands of high resolution and large cosmological volume remains challenging. Current high-resolution simulations that resolve individual supernova explosions are restricted to controlled simulations, and cosmological simulations treat bursty feedback as subgrid physics (E. Zhang et al. 2025; Y. Deng et al. 2024; J. Moreno et al. 2022; D. Nelson et al. 2019). Continued advances in simulations are therefore needed to clarify the formation processes and abundance of DMDGs.

#### ACKNOWLEDGMENTS

We thank Fangzhou Jiang and Hui Li for useful discussions. This work is supported in part by the National Key Research and Development Program of China (No. 2022YFF0503304), the National Science Foundation of China (No. 12588101), the New Cornerstone Science Foundation through the XPLORER PRIZE, the China Manned Space Program (No. CMS-CSST-2025-A03), the Project for Young Scientists in Basic Research of the Chinese Academy of Sciences (No. YSBR-092), the Postdoctoral Fellowship Program of CPSF (No. GZB20250738), and the Jiangsu Funding Program for Excellent Postdoctoral Talent (No. 2025ZB209).

#### APPENDIX

##### A. STAR FORMATION IN GAS REMNANTS

Our simulations reveal a systematic trend in which star formation is more efficient when the gravitational binding is weakened. To demonstrate this, we compare the quantity  $b_T$  for the  $\gamma = 1$  (left) and  $\gamma = 0.1$  (right) cases in Figure 5. This parameter, motivated by the ratio of dynamical time to free-fall time, increases with star formation efficiency.

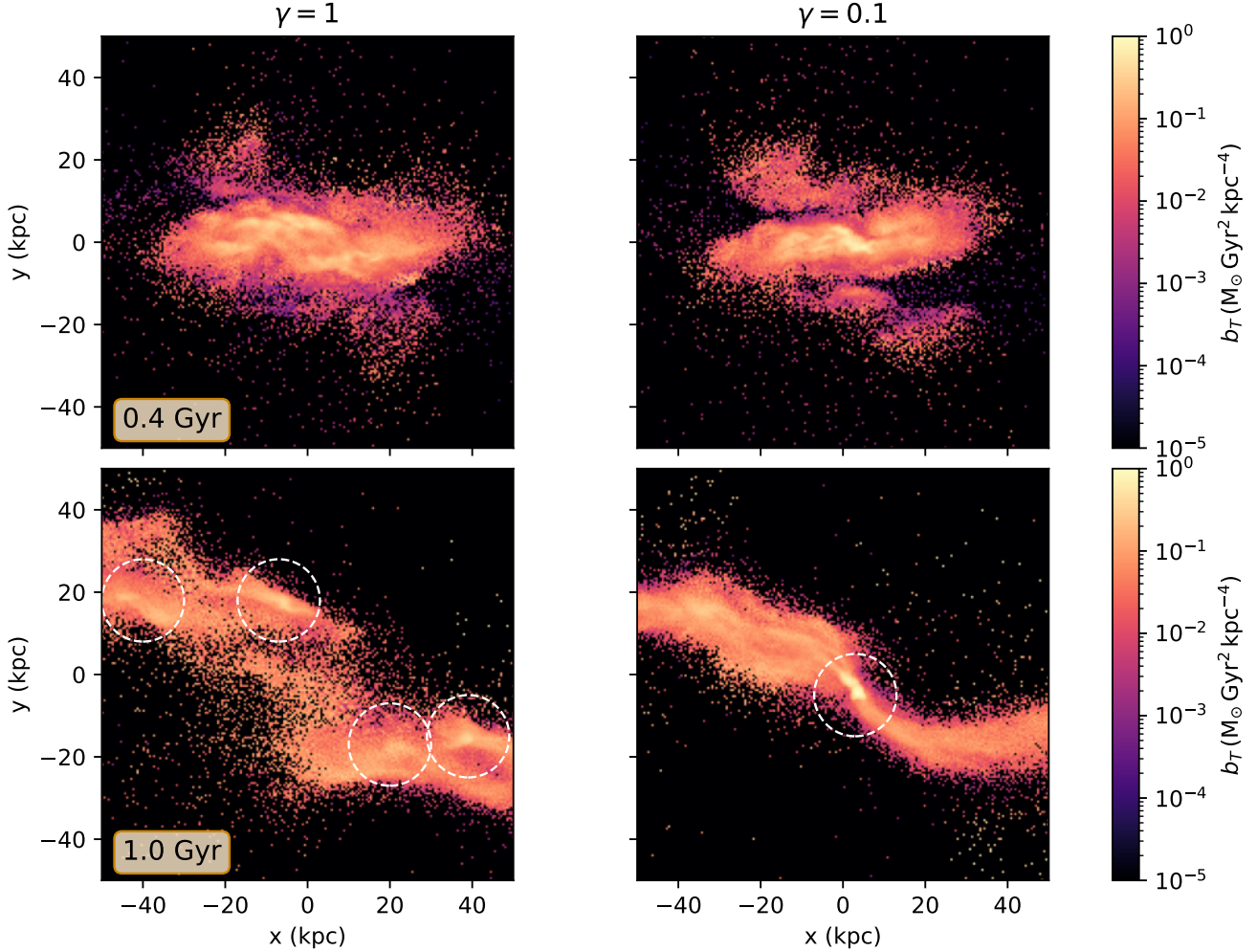


**Figure 5. Comparison of star formation efficiency in cored and cuspy benchmarks.** Maps of the  $b_T$ , which traces the star formation efficiency, are shown for the cuspy ( $\gamma = 1$ , 2a, left) and cored ( $\gamma = 0.1$ , 2b, right) benchmarks at  $t = 0.4$  Gyr (top) and 1.0 Gyr (bottom). White circles mark the sites of the forming DMDGs. The cored ( $\gamma = 0.1$ ) halo develops a significantly brighter region, indicating higher  $b_T$  values and enhanced star formation efficiency at the DMDG site. The cuspy ( $\gamma = 1$ ) halo, while forms four DMDGs, has substantially lower  $b_T$  values.

Following A. K. Leroy et al. (2016), we define

$$b_T \equiv \frac{\Sigma_{\text{gas}}}{\sigma_{v,\text{gas}}^2 + c_s^2} \propto \left( \frac{\tau_{\text{dyn}}}{\tau_{\text{ff}}} \right)^2, \quad (\text{A1})$$

with  $c_s = \sqrt{T k_B / (\mu m_p)}$  and  $\mu = 2.3$ .

Figure 5 shows  $b_T$  for the 2a benchmark ( $\gamma = 1$ , left panels) and the 2b benchmark ( $\gamma = 0.1$ , right panels) at  $t = 0.4$  Gyr (top) and 1.0 Gyr (bottom). The eventual locations of DMDG formation are enclosed by white circles. In the central collision region, the  $\gamma = 0.1$  case exhibits systematically higher  $b_T$ , corresponding to enhanced star formation. Moreover, in the  $\gamma = 1$  run the gas remnants fragment into three DMDGs, whereas in the  $\gamma = 0.1$  run only a single remnant forms. Similar behavior is observed across multiple paired simulations.

Figure 6 compares the mass evolution of the most massive DMDGs in the 2a ( $\gamma = 1$ ) and 2b ( $\gamma = 0.1$ ) simulations. In the weakened gravitational binding scenario ( $\gamma = 0.1$ ), efficient star formation produces a larger DMDG mass after the collision. Continued star formation beyond 2 Gyr steadily depletes the gas, leading to a decreasing gas fraction. In the  $\gamma = 1$  case, star formation also reduces the gas fraction, but with much lower efficiency, leaving a substantial

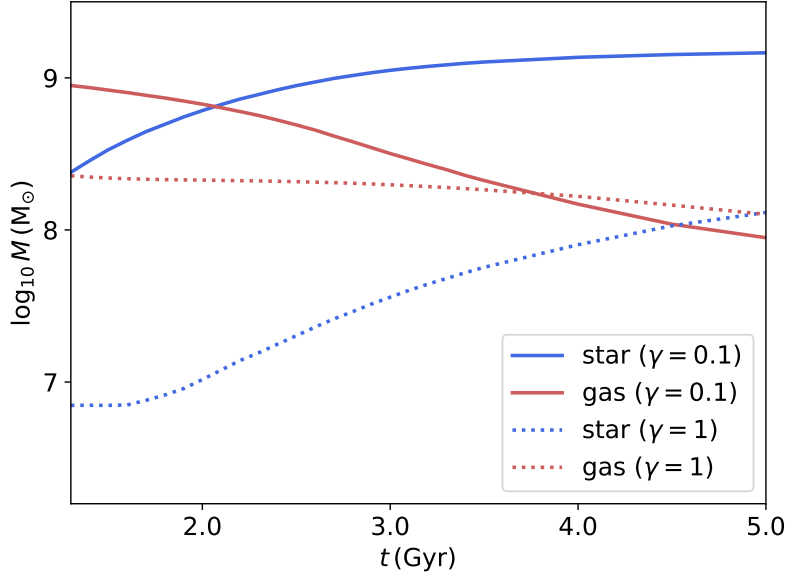


**Figure 6. Post-collision star formation.** Mass evolution of the most massive DMDGs in the 2a ( $\gamma = 1$ ) and 2b ( $\gamma = 0.1$ ) simulations. In the weakened binding case ( $\gamma = 0.1$ ), efficient star formation yields a more massive DMDG after the collision, with continued activity beyond 2 Gyr steadily depleting the gas reservoir. For  $\gamma = 1$ , star formation is much less efficient, leaving a substantial gas fraction even at 5 Gyr. In both scenarios, the total DMDG mass increases only modestly, from  $11 \times 10^8 \text{ M}_\odot$  ( $2.3 \times 10^8 \text{ M}_\odot$ ) to  $15 \times 10^8 \text{ M}_\odot$  ( $2.6 \times 10^8 \text{ M}_\odot$ ) in the  $\gamma = 0.1$  ( $\gamma = 1$ ) case.

gas reservoir even at 5 Gyr. In both cases, the total DMDG mass changes only modestly, increasing from  $11 \times 10^8 \text{ M}_\odot$  ( $2.3 \times 10^8 \text{ M}_\odot$ ) to  $15 \times 10^8 \text{ M}_\odot$  ( $2.6 \times 10^8 \text{ M}_\odot$ ) in the  $\gamma = 0.1$  ( $\gamma = 1$ ) simulation.

## B. STABILITY OF SIDM CORES

The SIDM benchmark in our study is implemented by incorporating cored halos obtained from a pre-simulation. Specifically, we use `Gadget-2` to evolve an initial system consisting of a gas disk and dark matter under gravity and SIDM ( $\sigma/m = 20 \text{ cm}^2 \text{ g}^{-1}$ ) for 2 Gyr. The final snapshot is then passed to `Gadget-4` to initialize the hydrodynamical collisional simulation. This strategy is justified by the following considerations.

First, radiation pressure in the gaseous disk is subdominant compared to gravitational support; therefore, running the initial SIDM simulation without hydrodynamics does not break the equilibrium of the gas disk, allowing it to be transferred consistently into a subsequent hydrodynamical run. Second, the constant SIDM cross section per mass adopted here should be regarded as an effective constant cross section (D. Yang & H.-B. Yu 2022). In velocity-dependent SIDM models consistent with observational constraints, the effect of SIDM during the collision can be neglected because the collision velocity is much larger than the typical particle velocities in the progenitor halos. Lastly, we assume that once SIDM cores form, the resulting cored profiles remain stable over relatively long timescales, even if SIDM interactions are subsequently turned off. This implies that SIDM halos reach a quasi-hydrostatic equilibrium, a point we explicitly verify with a toy simulation.

Figure 7 illustrates this verification for the progenitor system in the 1c simulation. During the first 2 Gyr, the halo evolves under SIDM: the dark matter core develops rapidly within the first  $\sim 1$  Gyr and then approaches a stable configuration. After 2 Gyr, SIDM is switched off and the simulation continues. Both the dark matter (red) and stellar (blue) components remain stable for at least another 2 Gyr. This demonstrates that neglecting SIDM in the collisional simulation is a valid approximation.

## C. TABULATED FULL SIMULATION RESULTS

We adopt the gas cooling and star formation module provided in the `Gadget-4` code. Radiative cooling is implemented through tabulated rates for primordial gas, while stars form stochastically from dense gas following the multiphase ISM prescription of V. Springel & L. Hernquist (2003). Although our study does not focus on the detailed dynamical processes within UDGs, the efficiency of gas cooling plays a key role in regulating their stability: a lower cooling rate

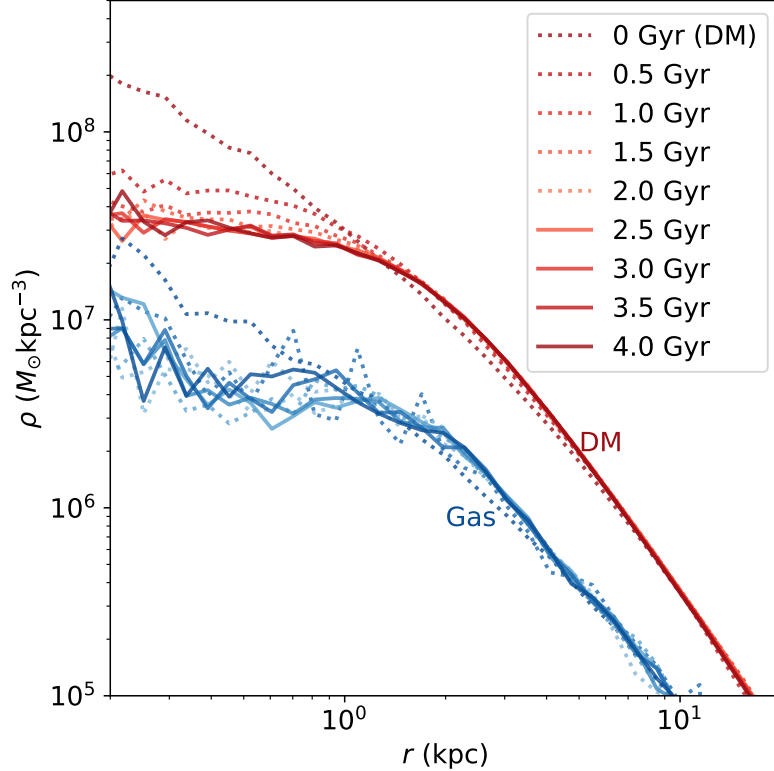


**Figure 7. Stability test of SIDM halos.** The progenitor system in the 1c simulation is first evolved under SIDM ( $\sigma/m = 20 \text{ cm}^2 \text{ g}^{-1}$ ) for 2 Gyr (dotted lines), when a dark matter core rapidly forms and reaches a stable configuration. SIDM interactions are then turned off and the system is further evolved for 2 Gyr (solid lines). Both the dark matter (red) and stellar (blue) components remain stable, confirming that the SIDM-induced core is long-lived and justifying the neglect of SIDM in the subsequent collisional simulations.

is generally expected to promote stability. To demonstrate that our conclusions are robust against variations in the cooling rate, we present the full simulation results in Table 2 for the default cooling rate and in Table 3 for a case with the cooling rate reduced by half. In these tables, we identify DMDGs as systems with  $M_*(r < 10\text{kpc}) > 10^6 M_\odot$ , reporting their abundance as well as the mass content of the most massive DMDGs in each simulation.

Figure 8 summarizes the reduced cooling case, in the same format as Figure 4 in the main text. All key features, most notably the enhancement in DMDG mass and star formation efficiency, remain unaffected. A comparison of the numerical results across the two tables shows that reduced cooling produces more DMDGs with lower characteristic masses. This indicates a potential degeneracy between the effects of gas cooling and weakened gravitational binding. The degeneracy can be resolved by the observed abundance of UDGs, which provides a means to constrain gas cooling (Y. Rong et al. 2017; R. F. J. van der Burg et al. 2017; A. Di Cintio et al. 2017; M. G. Jones et al. 2018).

Both Figure 4 and Figure 8 present results for the most massive DMDGs. To further illustrate the robustness of our findings, Figure 9 shows the total DMDG masses for the default cooling scenario. In all cases, the trend of enhanced DMDG masses in the weakened gravitational binding scenario remains unchanged.

## REFERENCES

Acevedo, J. F., An, H., Boukhtouchen, Y., et al. 2024, PhRvD, 110, 083004, doi: [10.1103/PhysRevD.110.083004](https://doi.org/10.1103/PhysRevD.110.083004)

Behroozi, P. S., Wechsler, R. H., & Conroy, C. 2013, ApJ, 770, 57, doi: [10.1088/0004-637X/770/1/57](https://doi.org/10.1088/0004-637X/770/1/57)

Binney, J., & Tremaine, S. 2008, Galactic Dynamics: Second Edition

Bournaud, F., & Duc, P. A. 2006, Astron. Astrophys., 456, 481, doi: [10.1051/0004-6361:20065248](https://doi.org/10.1051/0004-6361:20065248)

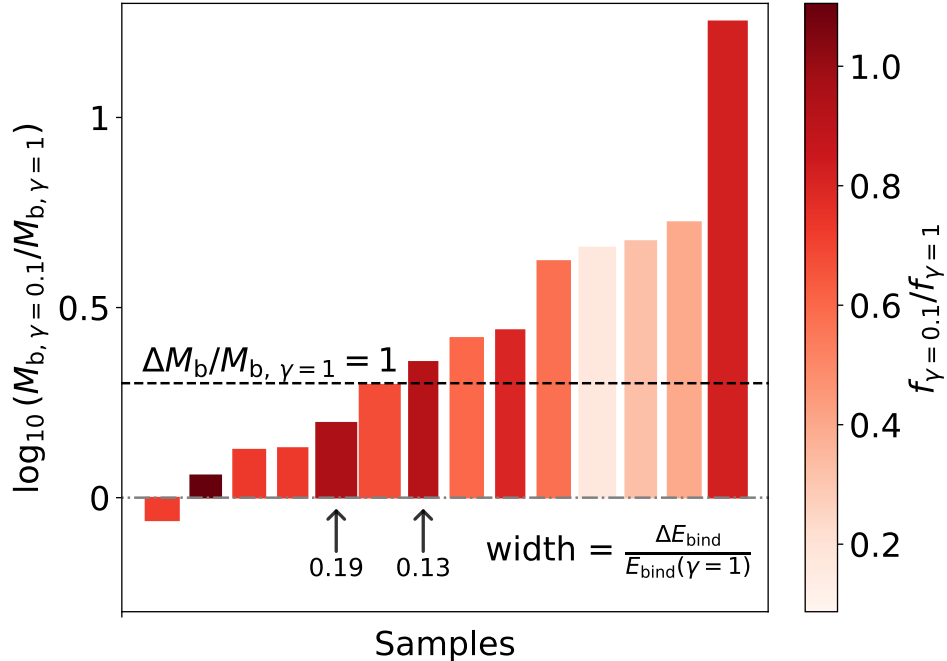


**Figure 8. Characteristics of the most massive DMDGs in 14 paired simulations with reduced gas cooling.** The bar chart summarizes results from contrasting simulations with inner slopes  $\gamma = 0.1$  and  $\gamma = 1$ . Bars are arranged in ascending order of the DMDG mass ratio,  $M_{b,\gamma=0.1}/M_{b,\gamma=1}$ . The bar width scales with the relative change in binding energy,  $(E_{\text{bind},\gamma=1} - E_{\text{bind},\gamma=0.1})/E_{\text{bind},\gamma=1}$ , while the color indicates the gas fraction,  $f = M_{\text{gas}}/(M_{\text{gas}} + M_{\text{stars}})$ . In contrast, the increase in the DMDG masses is predominantly positive. In 8 out of the 15 simulations, this increase exceeds 100%, as reflected by the bars that rise above the line representing  $\Delta M_b/M_{b,\gamma=1} = 1$ .

Chan, T. K., Kereš, D., Wetzel, A., et al. 2018, MNRAS, 478, 906, doi: [10.1093/mnras/sty1153](https://doi.org/10.1093/mnras/sty1153)

Comerón, S., Trujillo, I., Cappellari, M., et al. 2023, A&A, 675, A143, doi: [10.1051/0004-6361/202346291](https://doi.org/10.1051/0004-6361/202346291)

Dekel, A., & Silk, J. 1986, ApJ, 303, 39, doi: [10.1086/164050](https://doi.org/10.1086/164050)

Deng, Y., Li, H., Liu, B., et al. 2024, A&A, 691, A231, doi: [10.1051/0004-6361/202450699](https://doi.org/10.1051/0004-6361/202450699)

Di Cintio, A., Brook, C. B., Dutton, A. A., et al. 2017, MNRAS, 466, L1, doi: [10.1093/mnrasl/slw210](https://doi.org/10.1093/mnrasl/slw210)

Di Cintio, A., Brook, C. B., Dutton, A. A., et al. 2017, Mon. Not. Roy. Astron. Soc., 466, L1, doi: [10.1093/mnrasl/slw210](https://doi.org/10.1093/mnrasl/slw210)

Di Cintio, A., Brook, C. B., Macciò, A. V., et al. 2014, MNRAS, 437, 415, doi: [10.1093/mnras/stt1891](https://doi.org/10.1093/mnras/stt1891)

Fox, P. J., Weiner, N., & Xiao, H. 2023, Phys. Rev. D, 108, 095043, doi: [10.1103/PhysRevD.108.095043](https://doi.org/10.1103/PhysRevD.108.095043)

Freundlich, J., Dekel, A., Jiang, F., et al. 2020, MNRAS, 491, 4523, doi: [10.1093/mnras/stz3306](https://doi.org/10.1093/mnras/stz3306)

Gentile, G., Famaey, B., Combes, F., et al. 2007, Astron. Astrophys., 472, L25, doi: [10.1051/0004-6361:20078081](https://doi.org/10.1051/0004-6361:20078081)

Governato, F., Brook, C., Mayer, L., et al. 2010, Nature, 463, 203, doi: [10.1038/nature08640](https://doi.org/10.1038/nature08640)

Graham, A. W., Merritt, D., Moore, B., Diemand, J., & Terzic, B. 2006, Astron. J., 132, 2685, doi: [10.1086/508988](https://doi.org/10.1086/508988)

Guo, Q., et al. 2019, Nature Astron., 4, 246, doi: [10.1038/s41550-019-0930-9](https://doi.org/10.1038/s41550-019-0930-9)

Hopkins, P. F., Keres, D., Onorbe, J., et al. 2014, Mon. Not. Roy. Astron. Soc., 445, 581, doi: [10.1093/mnras/stu1738](https://doi.org/10.1093/mnras/stu1738)

Jiang, F., Dekel, A., Freundlich, J., et al. 2019, Mon. Not. Roy. Astron. Soc., 487, 5272, doi: [10.1093/mnras/stz1499](https://doi.org/10.1093/mnras/stz1499)

Jing, Y., Wang, C., Li, R., et al. 2019, MNRAS, 488, 3298, doi: [10.1093/mnras/stz1839](https://doi.org/10.1093/mnras/stz1839)

Jones, M. G., Papastergis, E., Pandya, V., et al. 2018, A&A, 614, A21, doi: [10.1051/0004-6361/201732409](https://doi.org/10.1051/0004-6361/201732409)

Kaviraj, S., Darg, D., Lintott, C., Schawinski, K., & Silk, J. 2012, MNRAS, 419, 70, doi: [10.1111/j.1365-2966.2011.19673.x](https://doi.org/10.1111/j.1365-2966.2011.19673.x)

Keim, M. A., van Dokkum, P., Shen, Z., et al. 2025, Astrophys. J., 988, 165, doi: [10.3847/1538-4357/addfd4](https://doi.org/10.3847/1538-4357/addfd4)

Kong, D., Kaplinghat, M., Yu, H.-B., Fraternali, F., & Mancera Piña, P. E. 2022, ApJ, 936, 166, doi: [10.3847/1538-4357/ac8875](https://doi.org/10.3847/1538-4357/ac8875)

Koo, H. 2025, J. Korean Phys. Soc., 87, 430, doi: [10.1007/s40042-025-01420-8](https://doi.org/10.1007/s40042-025-01420-8)

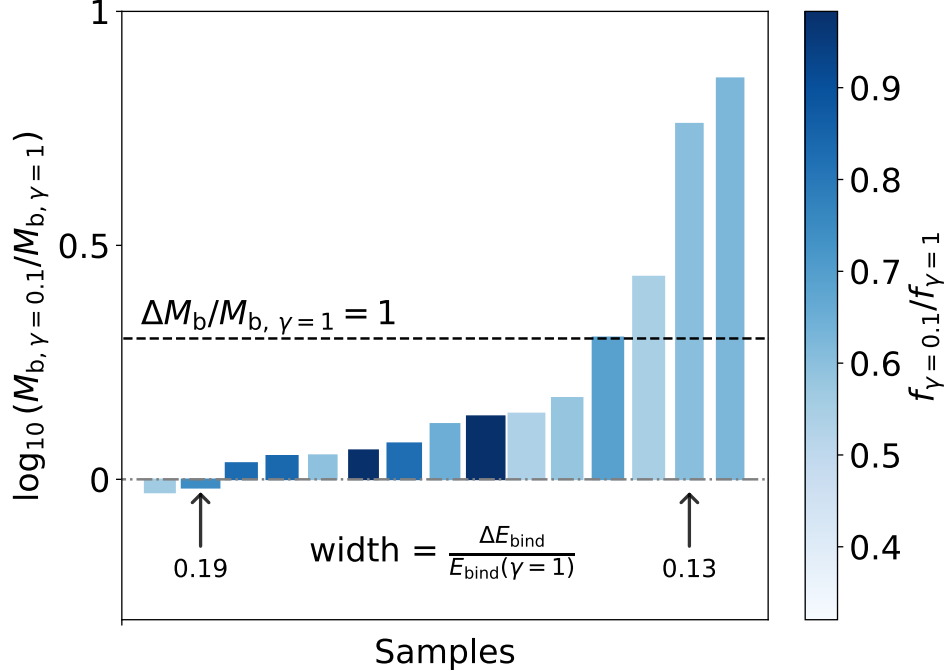


**Figure 9. Characteristics of the summed DMDG content for 15 paired simulations.** The bar chart summarizes results from contrasting simulations with inner slopes  $\gamma = 0.1$  and  $\gamma = 1$ . Bars are arranged in ascending order of the summed DMDG mass ratio,  $M_{b,\gamma=0.1}/M_{b,\gamma=1}$ . The bar width scales with the relative change in binding energy,  $(E_{\text{bind},\gamma=1} - E_{\text{bind},\gamma=0.1})/E_{\text{bind},\gamma=1}$ , while the color indicates the gas fraction,  $f = M_{\text{gas}}/(M_{\text{gas}} + M_{\text{stars}})$ . In contrast, the increase in the DMDG masses is predominantly positive. In 4 out of the 15 simulations, this increase exceeds 100%, as reflected by the bars that rise above the line representing  $\Delta M_b/M_{b,\gamma=1} = 1$ .

Kurapati, S., Chengalur, J. N., Kamphuis, P., & Pustilnik, S. 2020, MNRAS, 491, 4993, doi: [10.1093/mnras/stz3334](https://doi.org/10.1093/mnras/stz3334)

Lee, J., Shin, E.-j., Kim, J.-h., Shapiro, P. R., & Chung, E. 2024, ApJ, 966, 72, doi: [10.3847/1538-4357/ad2932](https://doi.org/10.3847/1538-4357/ad2932)

Leroy, A. K., Hughes, A., Schruba, A., et al. 2016, ApJ, 831, 16, doi: [10.3847/0004-637X/831/1/16](https://doi.org/10.3847/0004-637X/831/1/16)

Li, Z., Dekel, A., Mandelker, N., Freundlich, J., & François, T. L. 2023, MNRAS, 518, 5356, doi: [10.1093/mnras/stac3233](https://doi.org/10.1093/mnras/stac3233)

Mancera Piña, P. E., et al. 2020, Mon. Not. Roy. Astron. Soc., 495, 3636, doi: [10.1093/mnras/staa1256](https://doi.org/10.1093/mnras/staa1256)

Mashchenko, S., Couchman, H. M. P., & Wadsley, J. 2006, Nature, 442, 539, doi: [10.1038/nature04944](https://doi.org/10.1038/nature04944)

Medvedev, M. V. 2014, Phys. Rev. Lett., 113, 071303, doi: [10.1103/PhysRevLett.113.071303](https://doi.org/10.1103/PhysRevLett.113.071303)

Moreno, J., Danieli, S., Bullock, J. S., et al. 2022, Nature Astronomy, 6, 496, doi: [10.1038/s41550-021-01598-4](https://doi.org/10.1038/s41550-021-01598-4)

Navarro, J. F., Eke, V. R., & Frenk, C. S. 1996, Mon. Not. Roy. Astron. Soc., 283, L72, doi: [10.1093/mnras/283.3.L72](https://doi.org/10.1093/mnras/283.3.L72)

Nelson, D., Springel, V., Pillepich, A., et al. 2019, Computational Astrophysics and Cosmology, 6, 2, doi: [10.1186/s40668-019-0028-x](https://doi.org/10.1186/s40668-019-0028-x)

Ogiya, G. 2018, MNRAS, 480, L106, doi: [10.1093/mnrasl/sly138](https://doi.org/10.1093/mnrasl/sly138)

Papastergis, E., Adams, E. A. K., & Romanowsky, A. J. 2017, A&A, 601, L10, doi: [10.1051/0004-6361/201730795](https://doi.org/10.1051/0004-6361/201730795)

Peirani, S., Dubois, Y., Volonteri, M., et al. 2017, MNRAS, 472, 2153, doi: [10.1093/mnras/stx2099](https://doi.org/10.1093/mnras/stx2099)

Perret, V., Renaud, F., Epinat, B., et al. 2014, A&A, 562, A1, doi: [10.1051/0004-6361/201322395](https://doi.org/10.1051/0004-6361/201322395)

Piña Mancera, P. E., Fraternali, F., Oosterloo, T., et al. 2022, Mon. Not. Roy. Astron. Soc., 512, 3230, doi: [10.1093/mnras/stab3491](https://doi.org/10.1093/mnras/stab3491)

Pontzen, A., & Governato, F. 2012, MNRAS, 421, 3464, doi: [10.1111/j.1365-2966.2012.20571.x](https://doi.org/10.1111/j.1365-2966.2012.20571.x)

Rong, Y., Guo, Q., Gao, L., et al. 2017, MNRAS, 470, 4231, doi: [10.1093/mnras/stx1440](https://doi.org/10.1093/mnras/stx1440)

Sales, L. V., Navarro, J. F., Peñafiel, L., et al. 2020, MNRAS, 494, 1848, doi: [10.1093/mnras/staa854](https://doi.org/10.1093/mnras/staa854)

Shin, E.-j., Jung, M., Kwon, G., et al. 2020, ApJ, 899, 25, doi: [10.3847/1538-4357/aba434](https://doi.org/10.3847/1538-4357/aba434)

Spergel, D. N., & Steinhardt, P. J. 2000, Phys. Rev. Lett., 84, 3760, doi: [10.1103/PhysRevLett.84.3760](https://doi.org/10.1103/PhysRevLett.84.3760)

Springel, V., & Hernquist, L. 2003, Mon. Not. Roy. Astron. Soc., 339, 289, doi: [10.1046/j.1365-8711.2003.06206.x](https://doi.org/10.1046/j.1365-8711.2003.06206.x)

**Table 2.** Galaxy collision simulations with **Gadget-4**: initial collision configurations and properties of the resulting dark-matter-dominated galaxies (DMDGs).

BM	$M_{200, \text{DM}}$ ( $10^{10} M_\odot$ )	$M_{\text{gas}}$ ( $10^{10} M_\odot$ )	$v_r$ ( $\text{km s}^{-1}$ )	$R_s$ (kpc)	$c$	$\gamma$	$W/E_{\text{bind}}$	$n$	$M_{\text{star}}$ ( $10^8 M_\odot$ )	$M_{\text{gas}}$ ( $10^8 M_\odot$ )
1a	1.5	0.15	400	2	14	1	8.75	1	0.38	1.49
1b						0.1	7.58	1	8.61	4.85
1c	1.5	0.15	400	2	14	SIDM	9.47	1	0.46	2.97
2a	2	0.2	400	2	14	1	14.73	4	0.10	2.13
2b						0.1	12.49	1	6.09	6.72
3a	2	0.2	280	2	14	1	14.73	2	4.89	3.70
3b						0.1	12.49	1	16.80	4.97
4a	1.0	0.1	400	1.5	4	1	3.53	1	0.15	4.13
4b						0.1	2.87	1	0.30	5.54
5a	1.5	0.15	400	2	4	1	7.17	1	6.96	8.32
5b						0.1	5.82	1	9.61	5.05
6a	1.5	0.22	400	2	4	1	10.99	2	16.84	6.02
6b						0.1	9.28	1	20.70	7.03
7a	1.5	0.22	450	2	4	1	10.99	2	2.39	7.74
7b						0.1	9.28	2	3.23	3.96
8a	1.5	0.15	400	2	7	1	7.87	3	1.62	3.38
8b						0.1	6.47	1	11.15	3.91
9a	1.5	0.22	400	2	7	1	11.93	3	4.66	4.42
9b						0.1	10.21	2	18.33	5.57
10a	1.5	0.22	280	2	7	1	11.93	2	12.71	3.15
10b						0.1	10.21	1	25.90	7.27
11a	1.5	0.15	280	2	14	1	8.75	1	0.22	2.14
11b						0.1	7.58	1	8.38	5.20
12a	1.5	0.22	400	2	14	1	13.56	3	3.12	5.88
12b						0.1	11.68	1	13.15	5.23
13a	2	0.2	400	2	4	1	11.72	1	14.64	6.60
13b						0.1	9.75	1	19.49	5.88
14a	2	0.2	400	2	7	1	12.81	2	0.78	3.01
14b						0.1	10.83	1	13.97	5.53
15a	5	0.5	500	3.5	14	1	78.10	3	13.81	4.98
15b						0.1	66.40	1	26.08	5.11

NOTE—The properties listed are: (1) dark matter halo mass  $M_{200}$ , (2) total gas mass, (3) initial relative collision velocity  $v_r$ , (4) gaseous disk scale radius, (5) concentration  $c$ , (6)  $\gamma$ , (7) the absolute value of the baryonic binding energy  $|E_{\text{bind}}|$ , presented in unit  $E_0 \equiv (10^{12} M_\odot \text{ km}^2 \text{ s}^{-2})$ , (8) number of resulting DMDGs with  $M_b > 10^6 M_\odot$ , (9) stellar mass of the most massive DMDG, and (10) its gas mass. All properties are measured within 10 kpc at  $t = 2.0 \text{ Gyr}$ .

Springel, V., Pakmor, R., Zier, O., & Reinecke, M. 2021,  
MNRAS, 506, 2871, doi: [10.1093/mnras/stab1855](https://doi.org/10.1093/mnras/stab1855)

Toomre, A. 1964, ApJ, 139, 1217, doi: [10.1086/147861](https://doi.org/10.1086/147861)

Tulin, S., & Yu, H.-B. 2018, Physics Reports, 730, 1,  
doi: [10.1016/j.physrep.2017.11.004](https://doi.org/10.1016/j.physrep.2017.11.004)

Vale, A., & Ostriker, J. P. 2004, Mon. Not. Roy. Astron.  
Soc., 353, 189, doi: [10.1111/j.1365-2966.2004.08059.x](https://doi.org/10.1111/j.1365-2966.2004.08059.x)

van der Burg, R. F. J., Hoekstra, H., Muzzin, A., et al.  
2017, A&A, 607, A79, doi: [10.1051/0004-6361/201731335](https://doi.org/10.1051/0004-6361/201731335)

van Dokkum, P., Danieli, S., Abraham, R., Conroy, C., &  
Romanowsky, A. J. 2019, ApJL, 874, L5,  
doi: [10.3847/2041-8213/ab0d92](https://doi.org/10.3847/2041-8213/ab0d92)

van Dokkum, P., Danieli, S., Cohen, Y., et al. 2018, Nature,  
555, 629, doi: [10.1038/nature25767](https://doi.org/10.1038/nature25767)

van Dokkum, P., Shen, Z., Keim, M. A., et al. 2022,  
Nature, 605, 435, doi: [10.1038/s41586-022-04665-6](https://doi.org/10.1038/s41586-022-04665-6)

Vogelsberger, M., Zavala, J., Schutz, K., & Slatyer, T. R.  
2019, Mon. Not. Roy. Astron. Soc., 484, 5437,  
doi: [10.1093/mnras/stz340](https://doi.org/10.1093/mnras/stz340)

**Table 3.** Same as Table 2, but with the cooling rate reduced by half.

BM	$M_{200, \text{DM}}$ ( $10^{10} M_\odot$ )	$M_{\text{gas}}$ ( $10^{10} M_\odot$ )	$v_r$ (km s $^{-1}$ )	$R_s$ (kpc)	$c$	$\gamma$	$W/E_{\text{bind}}$	$n$	$M_{\text{star}}$ ( $10^8 M_\odot$ )	$M_{\text{gas}}$ ( $10^8 M_\odot$ )
1a	1.5	0.15	400	2	14	1	8.75	2	0.02	1.14
1b						0.1	7.58	3	0.29	2.35
2a	2	0.2	400	2	14	1	14.73	5	0.02	1.02
2b						0.1	12.49	3	2.08	2.28
3a	2	0.2	280	2	14	1	14.73	4	3.43	2.97
3b						0.1	12.49	2	12.49	4.35
4a	1.0	0.1	400	1.5	4	1	3.53	2	0.06	0.55
4b						0.1	2.87	3	0.15	0.81
5a	1.5	0.15	400	2	4	1	7.17	2	0.35	2.29
5b						0.1	5.82	2	2.33	2.90
6a	1.5	0.22	400	2	4	1	10.99	1	10.56	7.62
6b						0.1	9.28	2	11.29	4.56
8a	1.5	0.15	400	2	7	1	7.87	2	0.04	0.26
8b						0.1	6.47	1	1.64	3.73
9a	1.5	0.22	400	2	7	1	11.93	3	0.49	2.96
9b						0.1	10.21	2	12.68	3.64
10a	1.5	0.22	280	2	7	1	11.93	2	21.53	5.88
10b						0.1	10.21	1	23.94	7.44
11a	1.5	0.15	280	2	14	1	8.75	2	3.67	2.79
11b						0.1	7.58	1	11.84	5.98
12a	1.5	0.22	400	2	14	1	13.56	4	1.69	3.53
12b						0.1	11.68	3	3.72	3.33
13a	2	0.2	400	2	4	1	11.72	3	0.75	3.64
13b						0.1	9.75	1	18.53	1.44
14a	2	0.2	400	2	7	1	12.81	2	0.19	1.91
14b						0.1	10.83	2	7.72	3.42
15a	5	0.5	500	3.5	14	1	78.10	5	16.31	4.45
15b						0.1	66.40	4	23.62	4.14

Williamson, D., Martel, H., & Romeo, A. B. 2016, ApJ, 831, 1, doi: [10.3847/0004-637X/831/1/1](https://doi.org/10.3847/0004-637X/831/1/1)

Yang, D., Nadler, E. O., & Yu, H.-B. 2023, Astrophys. J., 949, 67, doi: [10.3847/1538-4357/acc73e](https://doi.org/10.3847/1538-4357/acc73e)

Yang, D., & Yu, H.-B. 2022, JCAP, 2022, 077, doi: [10.1088/1475-7516/2022/09/077](https://doi.org/10.1088/1475-7516/2022/09/077)

Yang, D., & Yu, H.-B. 2022, JCAP, 09, 077, doi: [10.1088/1475-7516/2022/09/077](https://doi.org/10.1088/1475-7516/2022/09/077)

Yang, D., Yu, H.-B., & An, H. 2020, Phys. Rev. Lett., 125, 111105, doi: [10.1103/PhysRevLett.125.111105](https://doi.org/10.1103/PhysRevLett.125.111105)

Zaragoza-Cardiel, J., Smith, B. J., Jones, M. G., et al. 2024, A&A, 689, A206, doi: [10.1051/0004-6361/202450349](https://doi.org/10.1051/0004-6361/202450349)

Zhang, E., Sales, L. V., Gutcke, T. A., et al. 2025, arXiv e-prints, arXiv:2510.02432, doi: [10.48550/arXiv.2510.02432](https://doi.org/10.48550/arXiv.2510.02432)

Zhang, Z.-C., Bi, X.-J., & Yin, P.-F. 2025a, Astrophys. J., 981, 89, doi: [10.3847/1538-4357/adaf9d](https://doi.org/10.3847/1538-4357/adaf9d)

Zhang, Z.-C., Bi, X.-J., & Yin, P.-F. 2025b, JCAP, 03, 031, doi: [10.1088/1475-7516/2025/03/031](https://doi.org/10.1088/1475-7516/2025/03/031)